

1 **Trends in Surface Equivalent Potential Temperature:**
2 *A more comprehensive metric for global warming and weather extremes*
3

4 Fengfei Song^{1,2}, Guang J. Zhang^{3*}, V. Ramanathan^{3*}, L. Ruby Leung²

5 ¹ Frontiers Science Center for Deep Ocean Multispheres and Earth System, Ocean University of
6 China, Qingdao, Shandong, China

7 ² Atmospheric Sciences and Global Change Division, Pacific Northwest National Laboratory,
8 Richland, Washington, USA

9 ³ Scripps Institution of Oceanography, University of California San Diego, La Jolla, California,
10 USA

11 *Corresponding authors

12 For Submission to *PNAS*

13 September 28, 2021

14 Revised December 10, 2021

15
16 **Corresponding authors:** V. Ramanathan (vramanathan@ucsd.edu) and Guang Zhang
17 (gzhang@ucsd.edu)

18
19 **Classification:** Physical Sciences; Earth, Atmospheric, and Planetary Sciences

20 **Keywords:** Global warming, surface equivalent potential temperature, atmospheric convection,
21 weather extremes
22

Trends in surface air temperature (SAT) is a common metric for global warming^{1,2}. Using observations and observationally driven models, we show that a more comprehensive metric for global warming and weather extremes is the trend in surface equivalent potential temperature, Θ_{sfc} , since it also accounts for the increase in atmospheric humidity and latent energy. From 1980 to 2019, while SAT increased by 0.79 °C, Θ_{sfc} increased by 1.48 °C globally and as much as 4 °C in the tropics. The increase in water vapor is responsible for the factor of 2 difference between SAT and Θ_{sfc} trends. Θ_{sfc} increased more uniformly (than SAT) between the mid latitudes of the southern hemisphere and the northern hemisphere, revealing the global nature of the heating added by greenhouse gases (GHGs). Trends in heat extremes and extreme precipitation are correlated strongly with the global/tropical trends in Θ_{sfc} . The tropical amplification of Θ_{sfc} is as large as the arctic amplification of SAT, accounting for the observed global positive trends in deep convection and a 20% increase in heat extremes. With unchecked GHG emissions, while SAT warming can reach 4.8 °C by 2100, the global mean Θ_{sfc} can increase by as much as 12 °C, with corresponding increases of 12 °C (median) to 24 °C (5% of grid points) in land surface temperature extremes, a 14 to 30-fold increase in frequency of heat extremes, a 40% increase in the energy available for tropical deep convection, and up to 60% increase in extreme precipitation.

Significance statement

The Earth has warmed up by 1.2 ± 0.1 °C since the pre-industrial era. The most common metric to measure the ongoing global warming is surface air temperature since it has long and reliable

observational records. However, surface air temperature alone does not fully describe the nature of global warming and its impact on climate and weather extremes. Here, we show that surface equivalent potential temperature, which combines the surface air temperature and humidity, is a more comprehensive metric not only for the global warming but also for its impact on climate and weather extremes including tropical deep convection and extreme heat waves. We recommend that it should be used more widely in future climate change studies.

The planet has warmed by 1.2 ± 0.1 °C from its pre-industrial values^{1,2,3}, three quarters of which occurred in the past 40 years mostly due to anthropogenic emissions of greenhouse gases (GHGs). Some extreme weather events in recent years have been attributed to this anthropogenic warming⁴. Attributing weather extremes to global warming is one of the major new developments in climate science⁴. In fact, the Bulletin of American Meteorological Society concluded in 2017⁵ that “we’re experiencing new weather, because we’ve made a new climate.” Weather extremes connect global warming directly to human health. More than 80% of the world’s land regions are experiencing increased heat extremes due to human-induced greenhouse gas forcing¹. According to UN data⁶, from 1995 to 2015, 90% of disasters were weather related, resulting in about 606,000 loss of lives and 4.1 billion people injured and left homeless, among other adverse impacts. The number of weather disasters doubled during 2005 -2014 compared with 1985-1994 while global warming is happening faster than the warming projected even a few years ago⁷.

Surface air temperature (SAT) has been a widely accepted climate variable used to evaluate global warming. However, SAT by itself does not fully reflect the effect of global warming on climate and weather extremes. The radiative heating of the surface and the atmosphere by

greenhouse gases (GHGs) forcing increases both air temperature, i.e., atmospheric internal energy, and humidity, i.e., latent energy. Two factors contribute to the humidity increase: 1) Increase in surface temperature, SAT, by GHGs increases evaporation of water vapor from the surface, and 2) a warmer atmosphere can hold more water vapor because of the exponential increase of saturation vapor pressure, e_s , with temperature. Both the increase in surface evaporation with SAT and the increase in e_s result from the Clausius-Clapeyron equation for saturation vapor pressure, e_s , which dictates that e_s increases by about 6% to 15% (depending on the temperature, Supplement Text 1) per degree of warming.

One of the most robust findings of most if not all climate model studies is that increase in SAT leads to increase in humidity¹. This was shown first in a climate model study⁸. It was subsequently shown with humidity and temperature observations^{9,10} that spatial (latitudinal) as well as temporal (seasonal to interannual) variations in the observed humidity also follow the temperature dependence dictated by the Clausius-Clapeyron equation. Thus, the humidity increase with temperature, known as the water vapor- temperature feedback, is a fundamental property of the climate system and it influences climate change in three major ways:

First, it amplifies the warming by a factor of 1.5 to 2^{8,10,11}. The humidity increase with temperature is just as important, if not more so, in determining the magnitude of global warming. Since water vapor is the dominant greenhouse gas in the atmosphere, the water vapor- temperature feedback amplifies the water vapor greenhouse effect which in turn amplifies the warming significantly.

Second, the latent heat released in the atmosphere, which is a primary driver of tropical convection and the general circulation, also increases with the warming because of the exponential increase of saturation vapor pressure with temperature.

Third, as shown in more detail in this study, the humidity increase with global warming and the associated increase in latent energy of the atmosphere play a major role in determining weather extremes. It has also led to more frequent and stronger extreme events such as heatwaves, hurricanes, convection storms and flash floods¹²⁻¹⁵.

In summary, the increase in humidity and latent energy with temperature is a fundamental property of both climate and climate change. Thus, a more comprehensive metric of climate change is the change in the surface equivalent potential temperature Θ_{e_sfc} , which is an integrated metric of both temperature and humidity changes. When multiplied by C_p , the specific heat of air at constant pressure (Supplement Text 2), Θ_{e_sfc} is equivalent to a fundamental energy quantity called moist enthalpy, which is the sum of the internal ($C_p T$) and latent energy possessed by surface air. At the surface, moist enthalpy is also referred to as moist static energy. We prefer the variable Θ_{e_sfc} (instead of enthalpy or moist static energy) since it can be readily compared with SAT in temperature units.

Θ_{e_sfc} is also a governing parameter for atmospheric convective instability, the depth of penetration of convective clouds, the depth of the tropical troposphere, the severity of heatwaves, and the onset of tropical rainfall, and it has been widely used to predict the location of monsoon rainfall¹⁶⁻¹⁷.

Both SAT and humidity increases also play a major role in how the warming translates into public health effects. For example, a useful predictor of health impacts associated with heatwaves is the surface wet-bulb globe temperature (WBGT), which is a measure of heat stress a human body can endure¹⁸⁻²⁰. A simplified WBGT that accounts for both the effect of temperature and humidity (see Methods) is highly correlated (99%) with the surface equivalent potential temperature Θ_{e_sfc} (Supplement Fig. 1).

In spite of the importance of Θ_{e_sfc} , to our knowledge, it has not received much attention outside the meteorology community; only one previous study examined its historical change during 1973-2003 based on observational datasets²¹. Here, we examine global warming and its related weather and climate extremes through the lens of Θ_{e_sfc} , a more comprehensive thermodynamic measure of global warming.

Results

Θ_{e_sfc} (See Methods for the calculation) is derived from independent data sets, including HadCRU²²⁻²⁴, NCEP1²⁵, ERA5²⁶, MERRA2²⁷ and JRA55²⁸ (see Methods for additional details of the datasets). We focus on the common period of 1980-2019, since most reanalysis data are available during this period and the bulk of the observed SAT and Θ_{e_sfc} trends since the pre-industrial era occurred during this period (Supplementary Fig. 2). Among them, HadCRU is derived directly from observations of SAT and surface humidity. The other four datasets are reanalysis products that assimilate observed SAT as well as observed atmospheric temperature and pressure in dynamical models to simulate water vapor and other variables. NCEP1 and MERRA2 are reanalysis datasets from the U.S., ERA5 is a recent European (ECMWF) reanalysis dataset and JRA55 is a Japanese reanalysis dataset.

The four reanalysis datasets have similar time evolution in SAT and Θ_{e_sfc} to the observations (HadCRU). The observations have a trend of 0.79 °C over the 40-year period, while the trends range from 0.56 to 0.76 °C in the four reanalysis datasets (Fig 1a). The magnitude of the Θ_{e_sfc} trends is significantly different from that of SAT. Θ_{e_sfc} has much larger temporal variations than SAT and the linear trend (1.48 °C) is roughly double that of SAT (0.79 °C) in the observations. Similar magnitudes have also been captured in the four reanalysis datasets. Θ_{e_sfc} variations consist of contributions from temperature and moisture ($\theta_e T$ and

θ_{e_M} , respectively; See Eqs. (2) and (3) in Method), which contribute about equally to the Θ_{e_sfc} trends (Supplementary Fig. 3).

The geographical pattern of warming in terms of the SAT trend during 1980-2019 shows three prominent features: larger warming in northern hemisphere (NH) than southern hemisphere (SH), much larger mid-latitude to polar warming than tropical warming in NH, and enhanced warming over land relative to oceans (Fig. 2; Supplementary Fig. 4), all of which have been well documented^{1,2}. However, all of these three warming contrasts are significantly weakened when measured in Θ_{e_sfc} (Fig. 2). In other words, the Earth is heated more uniformly when measured by Θ_{e_sfc} . In Table 1, we quantify these differences of SAT and Θ_{e_sfc} by showing the warming ratios between NH and SH, between land and ocean, and between tropical and NH polar region. The warming trend in NH and land is roughly twice (2.19 and 1.91 respectively) as much as that in SH and in oceans in the observations measured by SAT. But the NH-SH contrast and land-ocean contrast in Θ_{e_sfc} trend is reduced to 1.58 and 1.24, respectively. When measured by SAT, the tropical warming is only 31% of the NH polar warming, known as the Arctic amplification phenomenon, but Θ_{e_sfc} trend in the tropics is more than half of that in the Arctic. All these features are well captured in the reanalysis datasets and climate models forced by observed sea surface temperature. Note that the NH/SH ratio in observations is quite different from reanalysis datasets and AMIP simulations. This is likely due to more missing values in SH than NH in observations. For future changes, the tropical amplification of the Θ_{e_sfc} trends is nearly comparable to the polar amplification of SAT in NH (Table S1).

Partitioning the Θ_{e_sfc} trends in terms of the temperature trends and moisture trends shows that the tropical and subtropical Θ_{e_sfc} trend is mainly contributed by the moisture

component ($\theta_e M$; Supplementary Fig. 5), which is due to the much larger increase of moisture. Most of the tropical and subtropical Θ_{e_sfc} increase occurs over ocean and tropical forests, including Amazon, Congo, and Maritime Continent, where there is abundant moisture. Because surface humidity observations are not regionally uniform, particularly over the oceans and in the southern hemisphere, we examine correlative satellite data (Fig. 3) to confirm the spatial patterns of the Θ_{e_sfc} trends. In addition, comparison with cloudiness and precipitation data from satellites reveals their direct link with the trend patterns of Θ_{e_sfc} . More specifically, the Θ_{e_sfc} trends illustrated by both the observations and reanalysis datasets are consistent with the trends in convection and cloud depth revealed by independent satellite datasets (Fig. 3). Corresponding to the maximum increase of nearly 4 °C in Θ_{e_sfc} over tropical marine locations and tropical forests, there is a decrease in outgoing longwave radiation at the top of the atmosphere due to increase in cloud top altitudes from deeper convection (Fig. 3b), an increase in precipitation (Fig. 3c) and an increase in cloud radiative forcing (Supplementary Fig.6a-b). These change patterns are well captured by climate models forced with observed sea surface temperatures (Supplementary Fig. 6c-f, Supplementary Fig. 7). The trends in convective available potential energy (CAPE) and the altitudes of convective cloud tops estimated from the reanalysis data (Supplementary Fig. 8) are consistent with the changes in outgoing longwave radiation, cloud radiative forcing and precipitation.

Besides the annual-mean precipitation change, during the satellite period another significant change in tropical rainfall is the emergence of its seasonal delay over land, with decreased rainfall in the spring and increased rainfall in the fall²⁹ (Supplementary Fig. 9a). The delayed onset of tropical rainfall annual cycle is a robust feature under global warming and is found to be linearly related to global warming³⁰⁻³². However, it is not well represented by the annual cycle of

SAT trend (Supplementary Fig. 9b). On the other hand, Θ_{e_sfc} trend shows a clear correspondence to the rainfall delay, with cooling during spring and warming during fall (Supplementary Fig. 9c). In short, the Θ_{e_sfc} trends are not only consistent among different observations and observationally constrained products and model simulations, but they also capture the global hydrological cycle changes much better than the SAT trends.

With unchecked emissions of greenhouse gases, the future changes of Θ_{e_sfc} can be even more pronounced. Here, we examine the Θ_{e_sfc} changes under the Representative Concentration Pathways 8.5 (RCP85) scenario based on 20 CMIP5 models (Supplementary Table 2). The ensemble average of SAT increases almost linearly with time, to 2 °C higher than the SAT for the pre-industrial era by 2039, and 4.8°C higher at the end of the 21st century (Fig. 4a). The extreme WBGT, which is defined as the 95th percentile of daily WBGT temperature (see Methods), in both tropical land and global land increase by close to 7°C by the end of the century relative to the pre-industrial era. Θ_{e_sfc} increases at an increasingly faster rate, reaching 4.9 °C and 12.5 °C higher than the pre-industrial era Θ_{e_sfc} by 2039 and the end of the 21st century, respectively. Similar to the linear trend pattern during 1980-2019 (Fig. 2a), future SAT warming also exhibits polar amplification and enhanced land-sea contrast (Supplementary Fig. 10a). In contrast, Θ_{e_sfc} warming is more uniform between land and ocean and subject to both polar and tropical amplifications (Fig. 4b), with the former dominated by the temperature component θ_{e_T} and the latter dominated by the moisture component θ_{e_M} (Supplementary Fig. 10). The regional changes by the end of the century can be as much as 16 °C in both the tropics and NH polar regions (Fig. 4b).

Implications for Extreme Weather

Examining climate change with the Thetae_sfc lens provides more insights into the links between warming and extreme weather. With unchecked emissions, global mean Thetae_sfc can increase by 12.5 °C in 2100 relative to the pre-industrial era. What do the huge increases in Thetae_sfc mean for extreme weather events? We describe three types of extremes below:

Deep Convection and tropical dynamics: Thetae_sfc has already been shown to be a good metric for deep convection (Fig. 3), as also demonstrated by much higher correlation with precipitation and CAPE than SAT (Supplementary Fig. 11 and 12), especially over land regions. More importantly, Thetae_sfc is much more tightly linked to extreme precipitation than SAT from both observations and climate model simulations over land (Fig. 5 and Supplementary Fig. 13), where most of the human activities take place. By the end of the century, with unchecked global warming, the intensity of model projected extreme precipitation can increase by 40 to 60% relative to current extreme precipitation (Supplementary Fig. 14). As extreme precipitation has a profound societal impact, this once again demonstrates the importance of using Thetae_sfc as a better metric for evaluating the impacts of global warming. Deep convection and the associated mesoscale and cirrus anvil cloud systems are the primary mechanisms by which latent heat is released to drive the large-scale tropical atmospheric circulation. They are linked to monsoon circulation, tropical hurricanes, and extensive high-level cirrus clouds³³⁻³⁴. With increased Thetae_sfc, the atmosphere is more convectively unstable, as measured by CAPE, and the maximum altitude a convective parcel from the surface can reach, a proxy for cloud top altitudes of convective clouds³⁵⁻³⁶, is higher (Supplementary Fig. 8). The tropical average (30°S-30°N) increases of CAPE and convection top height are 47 J/kg and 102 m during 1980-2019, respectively. These represent an 8.8% increase for CAPE and 1.4% increase for convection top height, relative to the climatological values of 1980-1999. By 2100, the 16 °C increase in

tropical Thetae_sfc can increase CAPE by more than 200 J/kg, over 30% increase relative to 1980-1999 (Supplementary Fig.15). The increase of CAPE in both observations and projected future climate can partly explain the increased rainfall extremes and severe thunderstorms³⁷⁻⁴⁰.

Extreme Heat Waves: Heatwaves, as measured by extremes (hottest 5% in daily mean values) in WBGT, are highly correlated with the tropical mean Thetae_sfc (Supplementary Fig. 17). In the past twenty years, the latest decade is warmer than the prior decade. Correspondingly, there is more extreme WBGT and higher tropical mean Thetae_sfc than the prior decade. The relationships between WBGT and tropical mean Thetae_sfc are very well captured by GCMs for both current and projected future climates (Supplementary Fig. 16b-c). For every 1°C change in tropical mean Thetae_sfc, there is a 0.4 to 0.5°C change in extreme WBGT, as inferred from the slopes in Supplementary Fig. 16. The ratio of the trend in WBGT extremes over land to that of the global mean Thetae_sfc is also highly concentrated at 0.5 for both current and future climates, more so for the latter (Supplementary Fig. 17). During 1980-2019, the relationship with the extreme WBGT trend is considerably higher in the mean Thetae_sfc trend than the mean SAT trend (with a correlation of 0.73 vs. 0.59; Fig. 6). As the global mean Thetae_sfc increases (Fig. 3a), future heat extremes become more severe (Supplementary Figs. 18 and 19). The extreme summer daily mean WBGT in different parts of the world (India, northern China, North America, and Europe) can increase by as much as 6 °C by the end of the 21st Century compared with the heat extremes in the current climate. Presently, extreme WBGT in many parts of the world (India, eastern China, eastern US and northern Australia, Supplementary Fig. 18) has already reached 32 °C, an extreme level of risk for outdoor activities²⁰. An increase in WBGT extremes by another 6 °C beyond the current extremes would be debilitating, particularly for the vulnerable population of 3 billion or more and for many ecosystems, as extreme WBGTs

exceeding 35 °C (approximately equal to human skin temperature) pose hazardous levels of risks to human health²⁰. The occurrence frequency of WBGT extremes exceeding 35 °C increases by 14 folds over India and southern China, 30 folds over northern China, 22 folds over North America and 23 folds over Europe by 2100 (Supplementary Fig. 19).

Concluding remarks

Thetae_sfc is often known as a measure of convective instability and the potential for atmospheric convection, but it has not yet been used to gauge global warming. In this study we showed that Thetae_sfc can be used as a metric, complementary to the widely used SAT, to measure global warming and its impact. SAT has the largest signal of global warming in high latitudes due to polar amplification. On the other hand, there are pronounced increases of Thetae_sfc in both the tropics and high latitudes as the Earth becomes warmer in observations and climate projection, owing to its inclusion of both temperature and moisture changes. The trends in Thetae_sfc match the trends in convection and cloud radiative forcing. More importantly, trends in mean Thetae_sfc are highly correlated with heatwave extremes both in the past and in future climate projection by models. Thetae_sfc is also tightly linked to extreme precipitation in both observations and global climate models. These findings suggest that Thetae_sfc complements SAT as a comprehensive metric of weather extremes caused by global warming and should be used more widely in future climate change studies.

Corresponding authors

Correspondence to V. Ramanathan (vramanathan@ucsd.edu) and Guang Zhang (gzhang@ucsd.edu).

Acknowledgements: This work is jointly supported by the U.S. Department of Energy, Office of Science, Biological and Environmental Research Program (BER) as part of the Earth System Model Development program area under Award Number DE-SC0022064 and National Science Foundation grant AGS-2054697 (G. Z.), U.S. Department of Energy Office of Science Biological and Environmental Research as part of the Regional and Global Model Analysis program area (F. S. and L. R. L.), Chinese Natural Science Foundation No. 42175029 (F. S.), and the Frieman endowed chair for climate sustainability (V. R.). PNNL is operated for the Department of Energy by Battelle Memorial Institute under contract DE-AC05-76RL01830. The work was initiated when F.S. was a postdoctoral researcher at Scripps Institution of Oceanography.

Author contributions

V.R. and G.Z. conceived the initial ideas, F.S. and G.Z. designed the research, F.S. performed the analysis. F.S., G.Z. and V.R. wrote the paper. All authors contributed to the interpretation of the results and the revision of the paper.

Competing interests.

Authors have no competing interests, financial or non-financial, to declare.

Method

1. Observational and reanalysis datasets

In this study, monthly surface air temperature (SAT) from HadCRUT4²² is used to represent the observed SAT, while monthly surface specific humidity and air temperature from HadISDH.blend version 1.1.1.2020f²³⁻²⁴ are used to calculate the surface equivalent potential temperature Θ_{e_sfc} (θ_e) based on the method shown in the Section 3. We refer to the SAT and θ_e as HadCRU, as both SAT and specific humidity are developed by the Climatic Research Unit (University of East Anglia) and the Hadley Centre (UK Met Office). We also use monthly SAT, surface specific humidity and surface pressure from the National Center for Environmental Prediction (NCEP)/National Center for Atmospheric Research (NCAR) reanalysis 1 (NCEP1)²⁵, ERA5²⁶, MERRA2²⁷ and JRA55²⁸ to calculate θ_e . For θ_e calculation in HadCRU, surface pressure is from NCEP1. Daily SAT and surface specific humidity from ERA5 during 1980-2019 are also used. The outgoing longwave radiation (OLR) from NOAA is used for the period of 1980-2019, which combines several satellite datasets⁴¹. The precipitation from GPCP is used for the period of 1980-2019⁴². The shortwave and longwave cloud radiative forcing (SWCRF and LWCRF, respectively) from ISCCP is used for the period 1984-2007⁴³. The reference period is chosen as 1980-1999 throughout the study to calculate the monthly anomalies, unless stated otherwise.

2. Model simulations

To obtain the future changes of θ_e , monthly mean outputs of SAT, surface specific humidity and surface pressure from historical and RCP8.5 simulations of 20 Coupled Model Intercomparison Project phase 5 (CMIP5; Ref. 44) models are used (see Supplementary Table 2). Except CESM1-

314 CAM5, daily mean outputs of SAT, surface specific humidity and surface pressure from
 315 historical and RCP8.5 simulations of these 20 models are also used. To assess the models' ability
 316 in capturing the current linear trends of convection, AMIP-type simulations from two models
 317 (CCSM4 and HadGEM2-A) are also used.

318 **3. Calculation of surface equivalent potential temperature**

319 We use the following simple formula based on Taylor expansion to calculate θ_e ⁴⁵:

$$320 \quad \theta_e \approx \left(T + \frac{L_v}{C_p} r \right) \left(\frac{p_0}{p_s} \right)^{\frac{R_d}{C_p}} \quad (1)$$

321 Here, T is the surface air temperature T_s , L_v is latent heat of vaporization (here it is taken as
 322 2500 kJ kg⁻¹), C_p is specific heat of dry air at constant pressure (here it is taken as 1005.7 J K⁻¹
 323 kg⁻¹), r is the mixing ratio, which is roughly equal to specific humidity q (it should be $r = \frac{q}{1-q}$ to
 324 be exact), p_0 is reference pressure (1000 hPa), p_s is surface pressure, R_d is specific gas constant
 325 for air (287.04 J K⁻¹ kg⁻¹). We can also divide θ_e into two components: one is linearly related to
 326 temperature (θ_{e_T}) and the other is related to moisture (θ_{e_M}). The two components are
 327 expressed as:

$$328 \quad \theta_{e_T} \approx T \left(\frac{p_0}{p_s} \right)^{\frac{R_d}{C_p}} \quad (2)$$

$$329 \quad \theta_{e_M} \approx \frac{L_v}{C_p} r \left(\frac{p_0}{p_s} \right)^{\frac{R_d}{C_p}} \quad (3)$$

330 Although θ_{e_M} is quite small compared to θ_{e_T} in terms of absolute values (50 K vs. 300 K),
 331 here, what matters is the temporal changes, which are comparable. According to the Clausius-
 332 Clapeyron equation and the relationship between saturation specific humidity and saturation
 333 vapor pressure, we can easily obtain the relationship between r and T as follows:

$$r = \frac{\epsilon R e_{s0}}{p} e^{\frac{L_v}{R_v} (\frac{1}{T_0} - \frac{1}{T})} \quad (4)$$

Here, ϵ is the ratio of the gas constants for dry air and water vapor (287 and 461 J K⁻¹ kg⁻¹, respectively), R is relative humidity, e_{s0} is vapor pressure at reference temperature T_0 (273.15 K), and R_v is gas constant for water vapor (461 J K⁻¹ kg⁻¹). Hence, θ_{e_M} can also be written as:

$$\theta_{e_M} \approx \frac{L_v \epsilon R e_{s0}}{c_p p} e^{\frac{L_v}{R_v} (\frac{1}{T_0} - \frac{1}{T})} \left(\frac{p_0}{p_s} \right)^{\frac{R_d}{c_p}} \quad (5)$$

In this form, θ_{e_M} is nonlinearly related to surface air temperature and increases faster with temperature at warmer temperatures.

4. Wet bulb globe temperature

The wet bulb globe temperature (WBGT) is a measure of heat stress in direct sunlight; it has been used by several western countries to provide guidance for military training and heavy labor activities in summer. The definition of WBGT involves sunlight incidence, wind speed, temperature and humidity, some of which are not available in archived observational data. Therefore, we use the simplified form from ref. 20:

$$WBGT = 0.567T + 0.393e + 3.94 \quad (6)$$

where T is temperature in Celsius, e is the vapor pressure of the air in hPa. The WBGT values at 28, 32, and 35 °C correspond to high, very high, and extreme risk to health²⁰.

5. Data availability

The data that support the findings of this study are available from the corresponding authors upon request. All data analyzed in the study are publicly available. HadCRUT4 dataset can be downloaded from the following website: <https://crudata.uea.ac.uk/cru/data/temperature/#datdow>.

354 HadISDH-blend version 1.1.1.2020f dataset can be downloaded from the following website:
355 <https://www.metoffice.gov.uk/hadobs/hadisdh/downloadblend1112020.html>. The NCEP1
356 reanalysis dataset is available at <https://psl.noaa.gov/data/gridded/data.ncep.reanalysis.html>. The
357 ERA5 reanalysis dataset can be downloaded from the following website:
358 <https://cds.climate.copernicus.eu#!/search?text=ERA5&type=dataset>. The MERRA2 reanalysis
359 dataset is available from https://gmao.gsfc.nasa.gov/reanalysis/MERRA-2/data_access/. The
360 JRA55 is available from <https://climatedataguide.ucar.edu/climate-data/jra-55>. The GPCP
361 precipitation dataset can be downloaded from the following website:
362 <https://psl.noaa.gov/data/gridded/data.gpcp.html>. The NOAA OLR dataset can be downloaded
363 from the following website: https://www.esrl.noaa.gov/psd/data/gridded/data.interp_OLR.html.
364 The ISCCP dataset can be downloaded from the following website:
365 https://eosweb.larc.nasa.gov/project/isccp/isccp_table. The global climate model outputs can be
366 obtained from the CMIP5 archive accessed through the following website: [http://www.ipcc-](http://www.ipcc-data.org/sim/gcm_monthly/AR5/Reference-Archive.html)
367 [data.org/sim/gcm_monthly/AR5/Reference-Archive.html](http://www.ipcc-data.org/sim/gcm_monthly/AR5/Reference-Archive.html).
368

References

1. Seneviratne, S. I., X. Zhang, M. Adnan, W. Badi, C. Dereczynski, A. Di Luca, S. Ghosh, I. Iskandar, J. Kossin, S. Lewis, F. Otto, I. Pinto, M. Satoh, S. M. Vicente-Serrano, M. Wehner, B. Zhou, 2021: Weather and Climate Extreme Events in a Changing Climate. In: *Climate Change 2021: The Physical Science Basis. Contribution of Working Group I to the Sixth Assessment Report of the Intergovernmental Panel on Climate Change* [Masson-Delmotte, V., P. Zhai, A. Pirani, S. L. Connors, C. Péan, S. Berger, N. Caud, Y. Chen, L. Goldfarb, M. I. Gomis, M. Huang, K. Leitzell, E. Lonnoy, J. B. R. Matthews, T. K. Maycock, T. Waterfield, O. Yelekçi, R. Yu and B. Zhou (eds.)]. Cambridge University Press. In Press.
2. NOAA National Centers for Environmental Information, State of the Climate: Global Climate Report for Annual 2020, online January 2021, retrieved on March 15, 2021 from <https://www.ncdc.noaa.gov/sotc/global/202013>.
3. World Meteorological Organization (2021): State of the Global Climate 2020, WMO-No. 1264, retrieved on December 1, 2021 from <https://public.wmo.int/en/our-mandate/climate/wmo-statement-state-of-global-climate>.
4. Herring, S. C., Christidis, N., Hoell, A., Hoerling, M. P., & Stott, P. A. (2021). Explaining Extreme Events of 2019 from a Climate Perspective, Bulletin of the American Meteorological Society, 102(1), S1-S116. Retrieved Jul 28, 2021, from <https://journals.ametsoc.org/view/journals/bams/102/1/BAMS-ExplainingExtremeEvents2019.1.xml>.

- 389 5. AMS News, 2017: [https://www.ametsoc.org/index.cfm/ams/about-ams/news/news-](https://www.ametsoc.org/index.cfm/ams/about-ams/news/news-releases/human-influence-on-climate-led-to-several-major-weather-extremes-in-2016/)
390 [releases/human-influence-on-climate-led-to-several-major-weather-extremes-in-2016/](https://www.ametsoc.org/index.cfm/ams/about-ams/news/news-releases/human-influence-on-climate-led-to-several-major-weather-extremes-in-2016/). Accessed
391 July 28th, 2021.
- 392 6. United Nations Office for Disaster Risk Reduction. (2015). *United Nations Office for Disaster*
393 *Risk Reduction (UNISDR)*. The Human cost of weather-related disasters 1995-2015.
394 [https://www.unisdr.org/2015/docs/climatechange/COP21_WeatherDisastersReport_2015_FINA](https://www.unisdr.org/2015/docs/climatechange/COP21_WeatherDisastersReport_2015_FINAL.pdf)
395 [L.pdf](https://www.unisdr.org/2015/docs/climatechange/COP21_WeatherDisastersReport_2015_FINAL.pdf) Accessed July 28th, 2021.
- 396 7. Xu, Y., V. Ramanathan, & D. G. Victor. Global warming will happen faster than we think.
397 *Nature*, 564, 30-32 (2018).
- 398 8. Manabe, S., and R. T. Wetherald, 1967: Thermal equilibrium of the atmosphere with a given
399 distribution of relative humidity. *J. Atmos. Sci.*, 24, 241-259, [https://doi.org/10.1175/1520-](https://doi.org/10.1175/1520-0469(1967)024<0241:TEOTAW>2.0.CO;2)
400 [0469\(1967\)024<0241:TEOTAW>2.0.CO;2](https://doi.org/10.1175/1520-0469(1967)024<0241:TEOTAW>2.0.CO;2)
- 401 9. Inamdar, A. K., and V. Ramanathan, 1998: Tropical and global scale interactions among water
402 vapor, atmospheric greenhouse effect and surface temperature, *J. Geophys. Res.*, 103, 32177-
403 32194.
- 404 10. Raval, A., and V. Ramanathan, 1989: Observational determination of the greenhouse effect,
405 *Nature*, 342, 758-761.
- 406 11. IPCC, 2007: Climate Change 2007: Synthesis Report. Contribution of Working Groups I, II
407 and III to the Fourth Assessment Report of the Intergovernmental Panel on Climate
408 Change [Core Writing Team, Pachauri, R.K and Reisinger, A. (eds.)]. IPCC, Geneva,
409 Switzerland, 104 pp.
- 410 12. Sobel A, et al. Human influence on tropical cyclone intensity. *Science*, 353, 242-246 (2016).

- 411 13. Emanuel, K. A., The dependence of hurricane intensity on climate, *Nature*, 326, 483–485,
412 (1987).
- 413 14. Habeeb, D. et al. Rising heat wave trends in large US cities. *Natural hazard*, 76 (3), 1651-
414 1665 (2015).
- 415 15. Prein, A.F., Liu, C., Ikeda, K. et al. Increased rainfall volume from future convective storms
416 in the US. *Nature Clim Change* 7, 880–884 (2017). <https://doi.org/10.1038/s41558-017-0007-7>.
- 417 16. Privé, N. C., & Plumb, R. A. Monsoon dynamics with interactive forcing. Part I:
418 Axisymmetric studies. *J. Atmos. Sci.* 64, 1417–1430 (2007).
- 419 17. Nie, J., Boos, W. & Kuang, Z. Observational evaluation of a convective quasi-equilibrium
420 view of monsoons. *J. Climate* 23, 4416–4428 (2010).
- 421 18. Ergonomics of the Thermal Environment—Assessment of Heat Stress Using the WBGT
422 (Wet Bulb Globe Temperature) Index ISO Standard No. 7243:2017 (International Organization
423 for Standardization, 2017); <https://www.iso.org/standard/67188.html>.
- 424 19. Zhang, Y., Held, I. & Fueglistaler, S. Projections of tropical heat stress constrained by
425 atmospheric dynamics. *Nat. Geosci.* 14, 133–137 (2021). [https://doi.org/10.1038/s41561-021-](https://doi.org/10.1038/s41561-021-00695-3)
426 00695-3.
- 427 20. Willett, K. M. & Sherwood, S. Exceedance of heat index thresholds for 15 regions under
428 warming climate using the wet-bulb globe temperature. *Int. J. Climatol.*, 32, 161-177 (2012).
- 429 21. Peterson, T. C., K. M. Willett, and P. W. Thorne (2011), Observed changes in surface
430 atmospheric energy over land, *Geophys. Res. Lett.*, 38, L16707, doi:10.1029/2011GL048442.

431 22. Morice, C.P., Kennedy, J.J., Rayner, N.A. & Jones, P.D. Quantifying uncertainties in global
432 and regional temperature change using an ensemble of observational estimates: the HadCRUT4
433 dataset. *Journal of Geophysical Research*, 117, D08101, doi:10.1029/2011JD017187 (2012).

434 23. Willett, K. M., Dunn, R. J. H., Thorne, P. W., Bell, S., de Podesta, M., Parker, D. E., Jones,
435 P. D. & Williams Jr., C. N.: HadISDH land surface multi-variable humidity and temperature
436 record for climate monitoring, *Clim. Past*, 10, 1983-2006, doi:10.5194/cp-10-1983-2014 (2014).

437 24. Freeman, E. et al. ICOADS Release 3.0: A major update to the historical marine climate
438 record. *Int. J. Climatol.* (2016).

439 25. Kalnay et al. The NCEP/NCAR 40-year reanalysis project, *Bull. Amer. Meteor. Soc.* 77,
440 437-470 (1996).

441 26. Hersbach, H., et al., (2020). The ERA5 global reanalysis. *Quart. J. Roy. Meteor. Soc.*,
442 <https://doi.org/10.1002/qj.3803>.

443 27. Gelaro, R., et al., (2017). The Modern-Era Retrospective Analysis for Research and
444 Applications, Version 2 (MERRA-2), *Journal of Climate*, 30(14), 5419-5454.

445 28. Kobayashi, S., Y. Ota, Y. Harada, A. Ebita, M. Moriya, H. Onoda, K. Onogi, H. Kamahori,
446 C. Kobayashi, H. Endo, K. Miyaoka, and K. Takahashi, 2015: The JRA-55 Reanalysis: General
447 specifications and basic characteristics. *J. Meteor. Soc. Japan*, 93, 5-48, doi:10.2151/jmsj.2015-
448 001.

449 29. Song, F., Leung, L.R., Lu, J. et al. Emergence of seasonal delay of tropical rainfall during
450 1979–2019. *Nat. Clim. Chang.* 11, 605–612 (2021). <https://doi.org/10.1038/s41558-021-01066->
451 x.

- 452 30. Biasutti, M. & Sobel, A. H. Delayed Sahel rainfall and global seasonal cycle in a warmer
453 climate. *Geophys. Res. Lett.* 36, L23707 (2009).
- 454 31. Song, F., Leung, L. R., Lu, J. & Dong, L. Seasonally dependent responses of subtropical
455 highs and tropical rainfall to anthropogenic warming. *Nat. Clim. Change* 8, 787–792 (2018).
- 456 32. Song, F., Lu, J., Leung, L. R. & Liu, F. Contrasting phase changes of precipitation annual
457 cycle between land and ocean under global warming. *Geophys. Res. Lett.* 47, e2020GL090327
458 (2020).
- 459 33. Smith, R. K., The role of cumulus convection in hurricanes and its representation in
460 hurricane models. *Rev. Geophys.*, **38**, 465–489, 2000.
- 461 34. Ramanathan, V. and W. D. Collins, Thermodynamic regulation of ocean warming by cirrus
462 clouds deduced from observations of 1987 El Nino. *Nature*, 351, 27-32, 1991.
- 463 35. Arakawa, A. & W. H. Schubert. Interaction of a cumulus cloud ensemble with the large-scale
464 environment, Part 1. *J. Atmos. Sci.*, 31, 674–701 (1974).
- 465 36. Zhang, G. J. & N. A. McFarlane. Sensitivity of climate simulations to the parameterization of
466 cumulus convection in the Canadian Climate Centre general circulation model. *Atmos.–Ocean*,
467 33, 407–446 (1995).
- 468 37. Lepore, C., D. Veneziano, A. Molini, Temperature and CAPE dependence of rainfall
469 extremes in the eastern United States, *Geophys. Res. Lett.*, 42, doi:10.1002/2014GL062247
470 (2015).
- 471 38. Seeley, J. D. Romps, The Effect of Global Warming on Severe Thunderstorms in the United
472 States, *J. Climate*, 28, 2443–2458, DOI: <https://doi.org/10.1175/JCLI-D-14-00382.1>. (2015).

473 39. Diffenbaugh, N., M. Scherer, and. R. Trapp, Robust increases in severe thunderstorm
 474 environments in response to greenhouse forcing, PNAS, 110, 16361-16366.
 475 www.pnas.org/cgi/doi/10.1073/pnas.1307758110 (2013).

476 40. Holland, G. and C. L. Bruyere, Recent intense hurricane response to global climate change.
 477 Clim. Dyn. 42, 617-627, <https://doi.org/10.1007/s00382-013-1713-0>, 2014.

478 41. Liebmann B. and C.A. Smith, 1996: Description of a Complete (Interpolated) Outgoing
 479 Longwave Radiation Dataset. Bulletin of the American Meteorological Society, 77, 1275-1277.

480 42. Adler, R. F. et al. The version 2 Global Precipitation Climatology Project (GPCP) monthly
 481 precipitation analysis (1979-present). J. Hydrometeor, 4(6), 1147-1167 (2003).

482 43. Rossow, W.B., and R.A. Schiffer, Advances in understanding clouds from ISCCP. Bull.
 483 Amer. Meteorol. Soc., 80, 2261-2288, doi:10.1175/1520-
 484 0477(1999)080<2261:AIUCFI>2.0.CO;2 (1999).

485 44. Taylor, K. E., Stouffer, R. J. & Meehl, G. A. An overview of CMIP5 and the experiment
 486 design. Bull. Am. Meteorol. Soc. 93, 485–498 (2012).

487 45. Stull, R. B. An Introduction to Boundary Layer Meteorology, Kluwer, 666 pp (1988).
 488

489 Table 1 The ratio of linear trend of SAT and Thetae_sfc in the observation, average of four
 490 reanalysis datasets and average of two AMIP runs during 1980-1999.

Data	Land/Ocean ratio		NH/SH ratio		Tropics/NH Polar ratio	
	SAT	Thetae_sfc	SAT	Thetae_sfc	SAT	Thetae_sfc
OBS	1.91	1.24	2.19	1.58	0.31	0.53
REA	2.17	1.68	2.94	2.80	0.24	0.42
AMIP	2.08	1.59	2.39	2.11	0.34	0.79

491

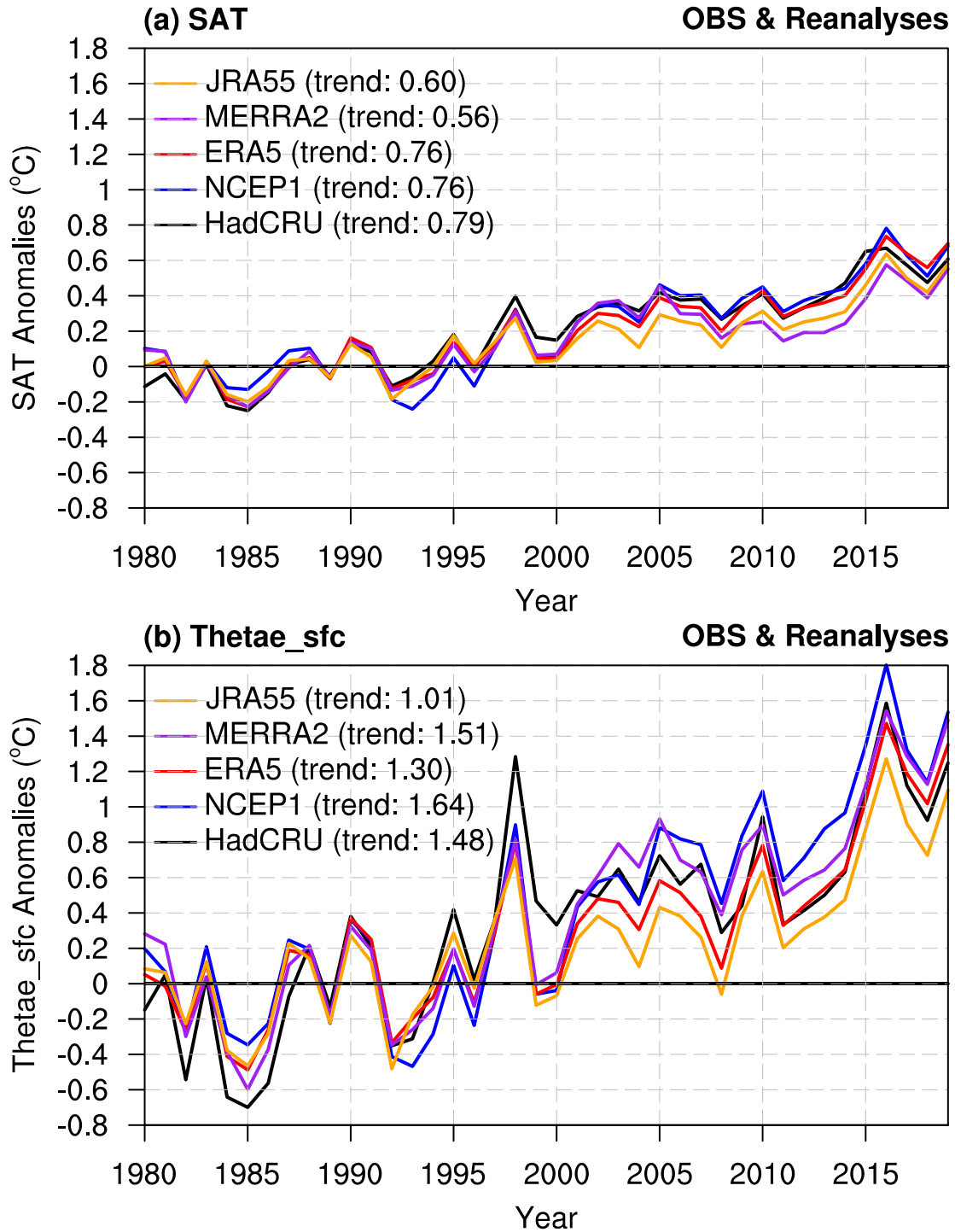


Figure 1 Time evolution of global mean surface air temperature (SAT; unit: °C) and surface equivalent potential temperature (Thetae_sfc; unit: °C). Annual-mean time series of (a) SAT anomalies and (b) Thetae_sfc anomalies from HadCRU (black line), NCEP1 (blue line), ERA5 (red line), MERRA2 (purple line) and JRA55 (orange line). The anomalies are with respect to 1980-1999 mean. The numbers in HadCRU and Reanalysis legends show the total warming during 1980-2019.

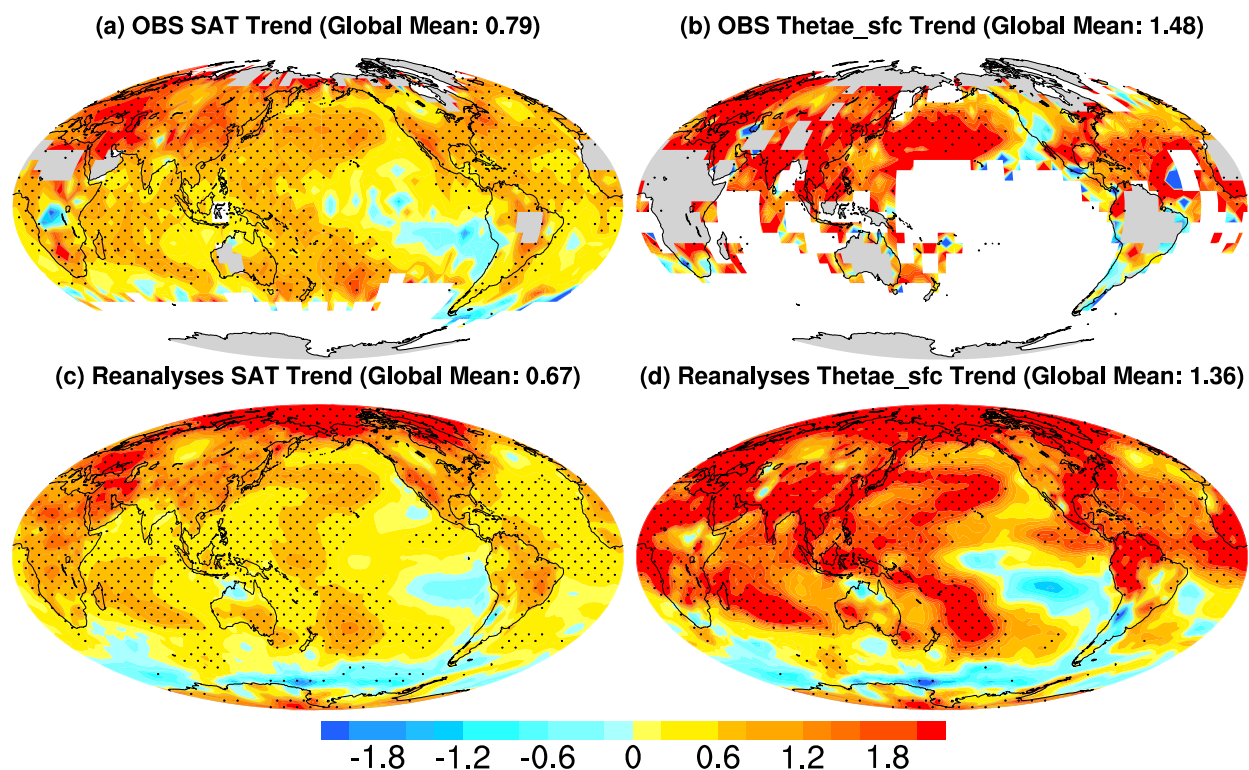
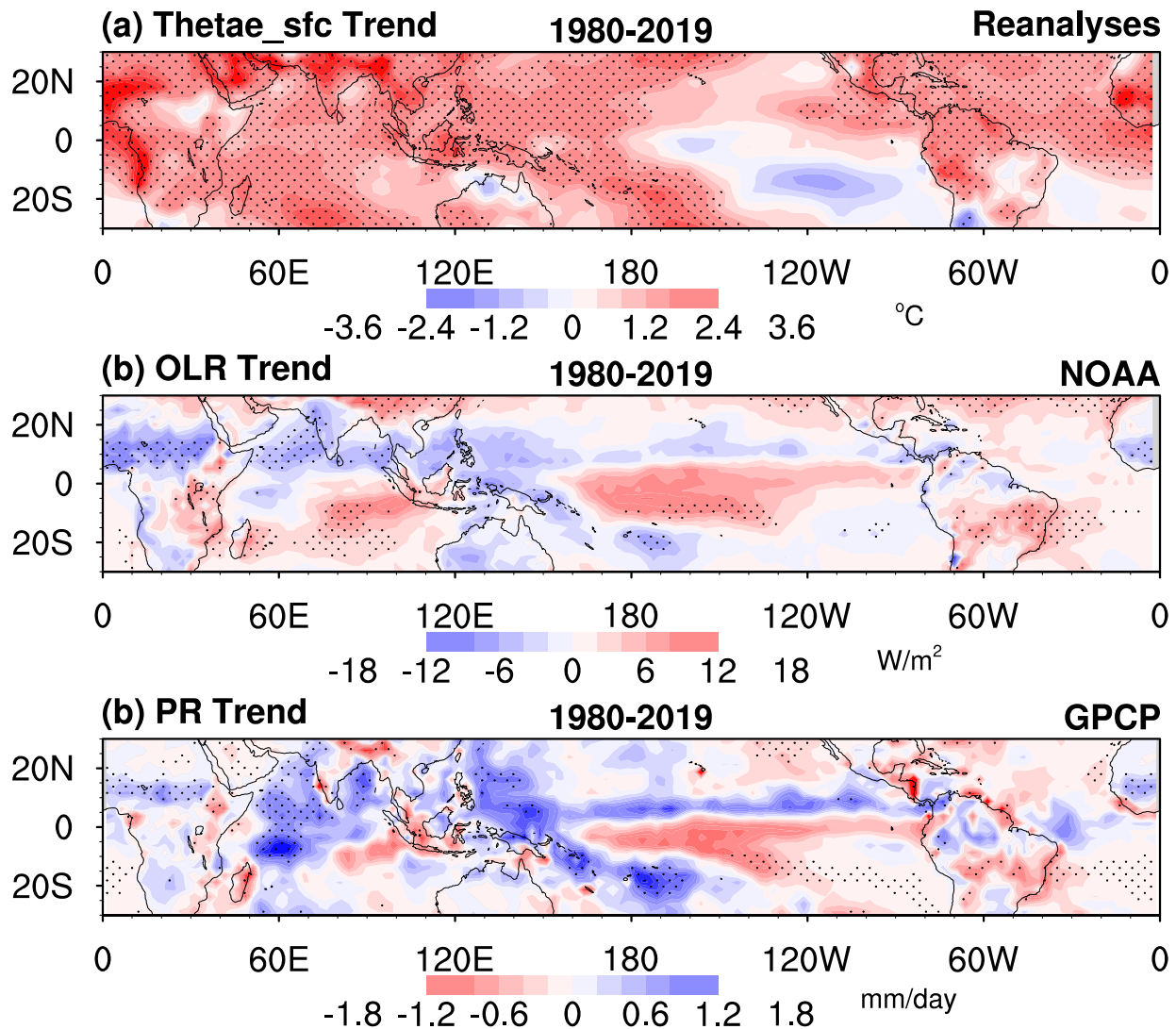


Figure 2 Global map of warming pattern in SAT and Thetae_sfc during 1980-2019. Linear trend of (a) SAT in OBS, (b) Thetae_sfc in OBS, (c) SAT in Reanalyses and (d) Thetae_sfc in Reanalyses. The trend has been normalized by the global mean value shown in the title of each panel. Results in the Reanalyses are obtained by averaging over all four reanalysis datasets (NCEP1, ERA5, MERRA2 and JRA55).

505



506

507

508

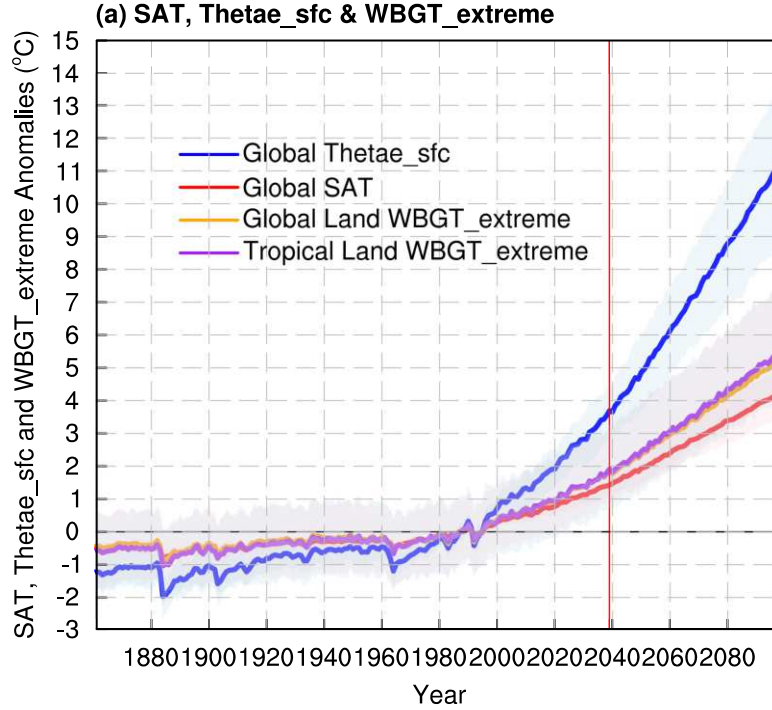
509

510

511

512

Figure 3 Changes of surface equivalent potential temperature (Thetae_sfc) in the tropics and its implication for convection. The spatial pattern of linear trend of annual-mean (a) Thetae_sfc (unit: °C) from the mean of four reanalysis datasets (NCEP1, ERA5, MERRA2 and JRA55), (b) outgoing longwave radiation (OLR; unit: W m^{-2}) from NOAA and (c) precipitation (unit: mm day^{-1}) from GPCP during 1980-2019. The stippled areas indicate that the linear trend is significant at the 5% level.



(b) Future Change of Thetae_sfc

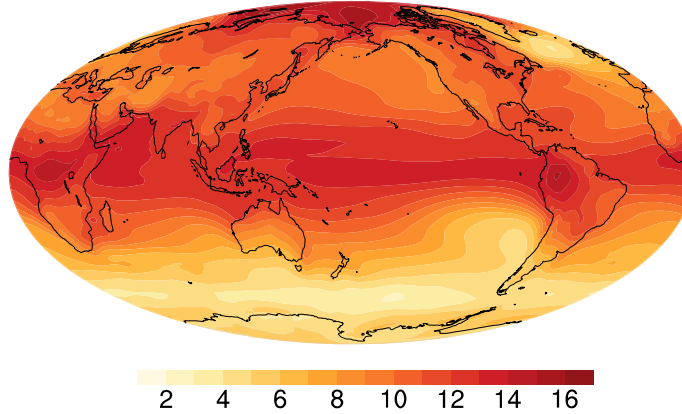


Figure 4 Future changes of surface air temperature (SAT) and surface equivalent potential temperature (Thetae_sfc). Annual-mean time series of (a) SAT (red line; unit: °C), Thetae_sfc (blue line; unit: °C), extreme WBGT over global land (orange line; unit: °C) and extreme WBGT over tropical land (purple line; unit: °C) anomalies relative to 1980-1999 mean and the future change patterns of (b) θ_e between future climate (2080-2099) and current climate (1980-1999). The shading indicates inter-model spread among 20 CMIP5 models.

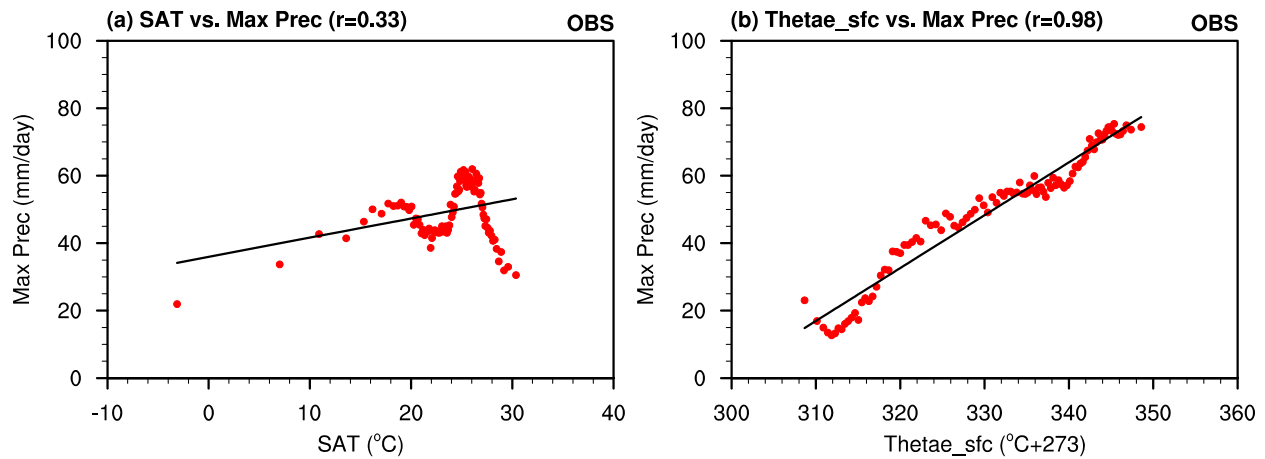


Figure 5 Relationship between annual maximum precipitation and annual mean SAT and Thetae_sfc over tropical land (30°S-30°N) during 1980-2019. The precipitation data is from NOAA Climate Prediction Center (CPC) gridded, gauge-based daily observations and SAT and Thetae_sfc are from ERA5 reanalysis. Each point represents a bin average of data from all land grid points in the latitude belt. The correlation coefficient is given in the parentheses at the top of each frame.

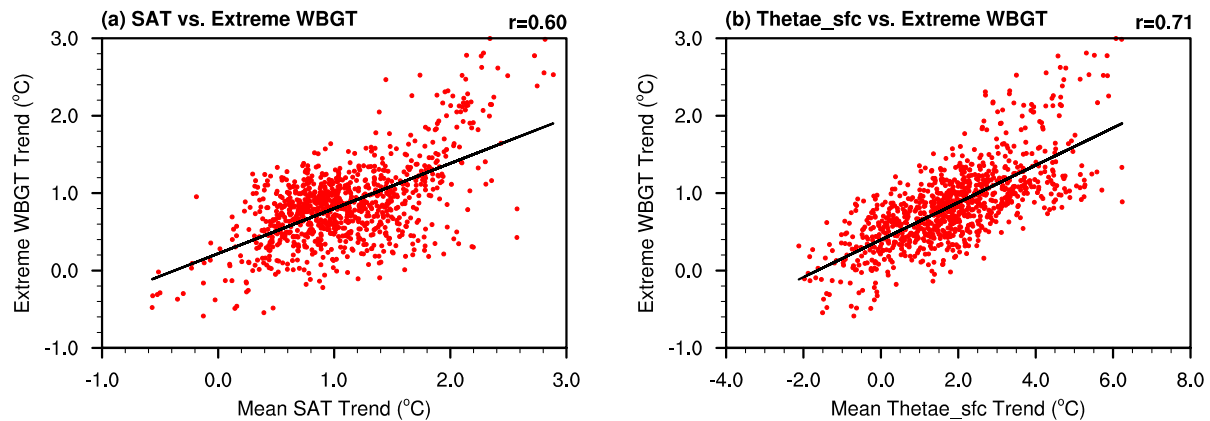


Figure 6 The extreme WBGT trend is highly correlated with mean Thetae_sfc trend over tropical land (30°S-30°N) during 1980-2019 in ERA5. Each data point represents one location.